Journal Name

ARTICLE

Synthesis of Hexagonal ZnO Nanodrums, Nanosheets and Nanowires by the Ionic Effect during the Growth of Hexagonal ZnO Crystalline

Mi-Hee Jung *, [a] and Moo-Jung Chu [a]

The hexagonal ZnO crystal has six nonpolar $(10\bar{1}0)$ prismatic faces that are capped by a polar Zn-terminated (0001) face or an O-terminated $(000\bar{1})$ face. The growth of a certain surface can be impeded by additives which preferentially adsorb onto specific crystal surfaces. By adding nonionic, anions and cations to a hexagonal ZnO precursor solution, we can synthesize hexagonal ZnO nanodrums, nanosheets and nanowires. The ZnO nanodrums are produced with a nonionic surfactant which forms a lamellar micelle structure in the solution. Hexagonal ZnO nanosheets were produced in the solution containing anion ions, which inhibited crystal growth in the c axis direction, whereas the cation ions accelerated the c axis crystal growth to produce ZnO nanowires. Thus, we could control the ZnO shape by controlling the ionic effect in the the hexagonal ZnO crystalline precursor solution. When the ZnO nanostructures was applied to the photovoltaic devices, ZnO nanowire solar cell shows the highest cell performance, which is the ideal structures to improve the performance of the photovoltaic devices.

1. Introduction

Zinc oxide (ZnO) has been widely investigated in applications such as ultraviolet nanolaser sources, gas sensors, solar cells, and field-emission display devices because it has a direct band gap of 3.37 eV and a large exciton binding energy of 60 meV.[1] Additionally, ZnO can easily be processed into various nanostructures, such as nanoparticles, nanowires, nanosheets and nanotubes, which have the unique features of photo-excited electron transport and light propagation due to light scattering or absorption. In particular, the one-dimensional (1D) structure of ZnO nanostructures have been the subject of much interest due to its multifunctionality, suggesting its potential for use in various applications, such as sensors, FETs, displays, solar cells, nanoscale generators, and piezoelectric materials. The thermodynamically stable phase for ZnO is zincite with the wurtzite (hcp) structure. The hexagonal ZnO crystal has both polar and non-polar faces. The six nonpolar $(10\bar{1}0)$ prismatic faces are capped by a polar Zn-terminated (0001) face or an O-terminated $(000\bar{1})$ face. The growth of a certain surface can be impeded by additives which preferentially adsorb onto a specific crystal surface.[2,3] The morphology of ZnO can be changed according to the growth rates of the surface, which can be kinetically controlled during the solution-phase synthesis process at moderate temperatures. If nonionic or ions (cations or anions) are absorbed at a favorable orientation approaching the polar faces to wurtzite ZnO (in contrast to the non-polar

faces) during the ZnO synthesis process, it has a noticeable effect on the morphology of ZnO, as the ZnO shape is determined by the difference in the growth rate due to the adsorption of counterions on the growing crystal faces.

In this study, we demonstrate the synthesis of a single-crystal hexagonal ZnO nanodrum, a ZnO nanosheet, and ZnO nanowire using a hexagonal ZnO precursor solution with the ionic effect at a low temperature. We added nonionic, anions and cations to the hexagonal ZnO precursor solution. These ions undergo different interactions with ZnO precursor ions, leading to the different ZnO morphology. On the basis of the structural information provided by an electron microscopy, we explain the growth mechanism for the formation of hexagonal ZnO nanodrums, nanosheets, and nanowire and the roles of the ions in the formation of the ZnO nanostructures during the hexagonal ZnO growth solution phase synthesis and then, we applied ZnO nanostructures to the solar cells to characterize the photovoltaic devices.
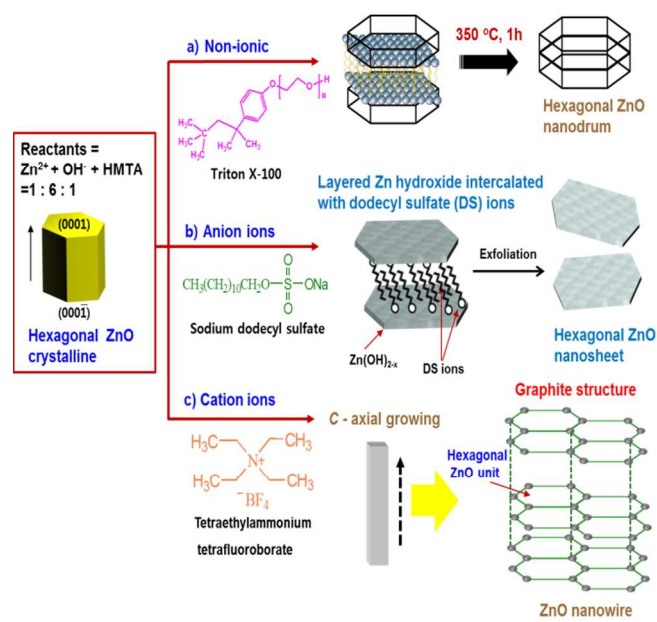
2. Results and discussion

One-dimensional hexagonal ZnO nanostructures are easily synthesized during low-temperature alkaline hydrothermal synthesis owing to the facile growth along the c axis of the wurtzite crystal, which has a hexagonal unit cell with six nonpolar $(10\bar{1}0)$ prismatic faces capped by polar oxygen $(000\bar{1})$ and zinc (0001) basal planes. The polar faces are

electrostatically unstable Tasker type III surfaces,[4] giving the (0001) planes the highest energy among all low-index surfaces. This suggests a growth habit in which the c- axis is the fastest growing direction (Figure 1). Therefore, hexagonal ZnO nanostructures could form and continue to develop by means of anisotropic growth. However, by introducing ions with preferential binding abilities onto ZnO crystal surfaces, the ZnO shape could change according to the direction of the ZnO growth. When we used a nonionic surfactant (Triton X-100) in conjunction with the ZnO hexagonal crystalline growth condition, two attached ZnO plates, designated as the ZnO nanodrum, was obtained because the nonionic surfactant, Triton X-100, forms self-assembled double layers and multilayers in lamellar micelles. The self-assembled Triton X-100 layers, which have both hydrophilic and hydrophobic properties, could


Figure 1. Proposed processes of structural changes from the hexagonal ZnO crystalline to hexagonal ZnO nanodrum, hexagonal nanosheet and nanowire. (a) ZnO hexagonal nanodrum formation process by the back-to-back stacking of the ZnO precursor on the lamellar micelle of a nonionic surfactant. (b) Structural model of a layered hexagonal ZnO nanosheet intercalated with dodecyl sulfate (DS) ions. (c) Graphite structure of ZnO nanowire formed by means of hexagonal ZnO unit stacking via a layer-by-layer process.

act as a template for the growth of ZnO. The hydrophilic head of OH^- can form an anionic surface exposed to water; thus, Zn^{2+} cations can directly attach to the negatively charged OH^- template to initiate the first layer of crystal growth. The produced $Zn(OH)_2$ can then be transformed into oxide through precipitation through a change in the temperature or the pH. The oxide can thereby form via a dissolution/precipitation or undergo a phase transformation.[2] The growth of the hexagonal ZnO nanodrum can take place simultaneously on both sides of the template and thus result in the back-to-back growth of paired disks. After removing the oil phase from the system, close attachment of the two disks at the smoother surfaces is energetically favorable due to the van der Waals interaction between the long tails of the self-assembled Triton X-100

monolayer on the surfaces (Figure 1a). Krishna et al.[5] reported that they fabricated a ZnO microdrum with hexagonally faceted twinned crystals having flat surfaces on both ends. They used the sodium salt of Aerosol-OT (NaAOT, sodium bis-(2-ethylhexyl) sulfosuccinate) as the surfactant. They followed a procedure similar to that reported by Wang et al.,[6] assuming that the ZnO microdrum was produced due to a change in the aging method. However, that method has the several parameters, such as the surfactant, the solvent and the molar ratio of Zn^{2+} to $NH_3 \cdot H_2O$ pertaining to the formation of the ZnO microdrum, as noted in the report of Wang et al.[6] In our work, the ZnO nanodrum was easily produced by the simple hexagonal ZnO precursor solution with a nonionic surfactant at a low temperature.

We also prepared a hexagonal ZnO nanosheet which was produced in the hexagonal ZnO precursor solution containing an anion surfactant, sodium dodecyl sulfate (SDS), which inhibited crystal growth in the c axis direction. Because SDS has negatively charged sulfonic acid groups in the chain, the anionic surfactant SDS will anchor onto the Zn^{2+}-terminated (0001) plane to suppress the c-axis growth due to the strong charge interaction. The adsorption of the SDS changes the nanocrystals, causing them to grow preferentially along the $(10\bar{1}0)$ direction to form stable and thin colloidal hexagonal nanoplates (Figure 1b). Dev et al.[7] reported that SDS plays an important role in controlling the lateral growth of the nanorods in a chemical solution. The most likely explanation for the formation of these sheets is the considerable crystal growth inhibition of the polar c faces by the sorption of SDS ions. The anionic surfactant SDS will anchor onto the Zn^{2+}-terminated (0001) plane to suppress the c-axis growth due to the strong charge interaction. Meanwhile, the reactivity of the $(000\bar{1})$ O^{2-}-terminated face was accounted for the lack of acid-base pairs on the oxygen polar face. Interaction between the SDS ions and the $(000\bar{1})$ face can occur at defect sites, i.e., at areas of exposed Zn^{2+} in steps or at oxygen vacancies. These structures have been proposed for SDS anion sorbing onto metal-oxide surfaces, *viz*. bridging, bidentate and unidentate.[8] The twinning phenomenon with the (0001) or $(000\bar{1})$ plane as the juncture occurs commonly in ZnO.[6,9] Given this result, we assumed that the ions of SDS are involved in the stabilization reaction on the $(000\bar{1})$ O^{2-}-terminated face on the counter side. The anion ions of SDS adsorb preferentially on the Zn^{2+}-terminated (0001) face and thus inhibit the crystal growth along the (0001) direction.

To observe the cation effect on the hexagonal ZnO growth condition, we added tetraethylammonium tetrafluoroborate (TEFB) to the zinc hydroxide and HMTA precursor solution. The cation of TEFB absorbed onto the specific site of the $(000\bar{1})$ O^{2-}-terminated face, which could indirectly promote growth in the c direction to produce the ZnO nanowire (Figure 1c). Due to the dangling bond configuration of the surfaces, the growth rate of face Zn^{2+}-terminated (0001) face on ZnO is faster than that of the $(000\bar{1})$ O^{2-}-terminated face on ZnO.[10] Each O atom on a Zn^{2+}-terminated (0001) face on the ZnO surface has three dangling bonds along the c axis, whereas each O atom on the

(000 $\bar{1}$) O^{2-}-terminated face has a single dangling bond. Therefore, the Zn stacking coefficient on the Zn^{2+}-terminated (0001) face is higher than that of the (000$\bar{1}$) O^{2-}-terminated face, making the growth rate of the Zn^{2+} terminated (0001) face of ZnO higher than that of the (000$\bar{1}$) O^{2-}-terminated face on ZnO. This produces the long length of ZnO, which is composed of a hexagonal ZnO unit. As shown in Figure 1c, the ZnO nanowire consists of stacked ZnO hexagonal subunits which are oriented and connected along the c axis of the growing crystallites, like the structure of graphite.

The morphological evolution was examined by FE-SEM. With the ionic effect of the surfactant, we could create various ZnO nanostructures. These results are shown in Figure 2-Figure 4. ZnO nanodrums are made up of hexagonally faceted twinned crystals having flat surfaces on both ends. The crystals are twinned on the (0001) plane (Figures 2a and 2b). The diameter and the height of the drums are around 400 nm and 350 nm, respectively. The electron diffraction pattern shows the single crystalline nature of each side of the drum. A TEM analysis of the hexagonal disk showed a single-crystal structure with (0001) top/bottom surfaces and (10$\bar{1}$0), (01$\bar{1}$0), ($\bar{1}$100) side facets (Figure 2c). TEM images of the faceted drums are also shown in Figure 2c.
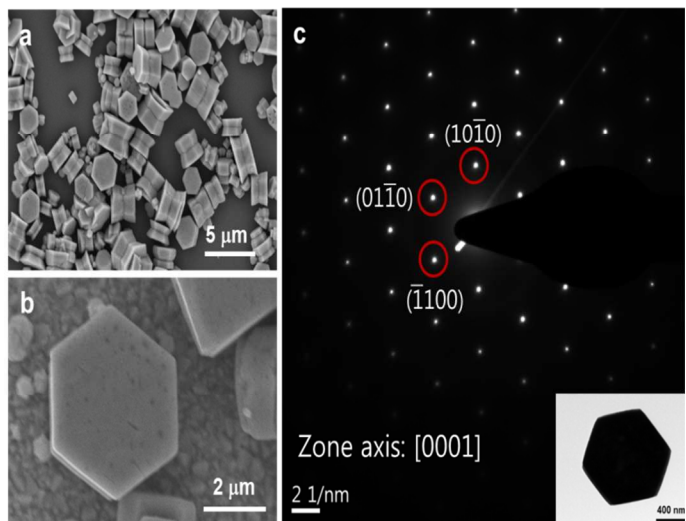
Figure 2. The (a) and (b) SEM images of the ZnO hexagonal nanodrum (c) (0001) zone axis SAED pattern obtained from the face of the ZnO nanodrum (incident electron beam normal to the ZnO nanodrum in b). The inset in (c) shows a TEM image of the ZnO nanodrum.

Figure 3 shows field-emission scanning electron microscopy (FE-SEM) images of the hexagonal ZnO nanosheet (Figure 3a). The average diameter of the hexagonal ZnO nanosheet is ~ 3.6 μm. In general, it is difficult to achieve uniformity of a lateral shape in nanosheets, as this requires a layer-by-layer (LBL) process, the Langmuir-Blodgett (LB) technique[11] and an additional exfoliation process.[12] In this result, we show a hexagonal ZnO nanosheet with a homogeneous thickness as prepared by the exfoliation of layered ZnO intercalated with dodecyl sulfate (DS) ions. Therefore, the hexagonal ZnO nanosheet was not stacked against other such sheets due to

electrostatic repulsion (Figure 3b). The hexagonal ZnO nanosheet is formed through the mesoscale assembly of hexagonal nanoparticle building units and consisted of many small particles. High-resolution TEM characterization and electron diffraction of individual nanostructures indicate that the hexagonal ZnO nanosheet consisted of particulate grains forming a hexagonal nanosheet on the order of hundreds of nanometers. These grains are built up from individual hexagonal ZnO crystals with diameters of 10-20 nm which are intrinsically interconnected to each other (Figure 3c). Figure 3d shows typical AFM images of the nanosheets. The thickness of the nanosheets was measured to be 10 nm. In general, the thickness observed by AFM is larger than that estimated from crystallographic data due to the absorption of water and DS ions as well as other systematic factors in the AFM
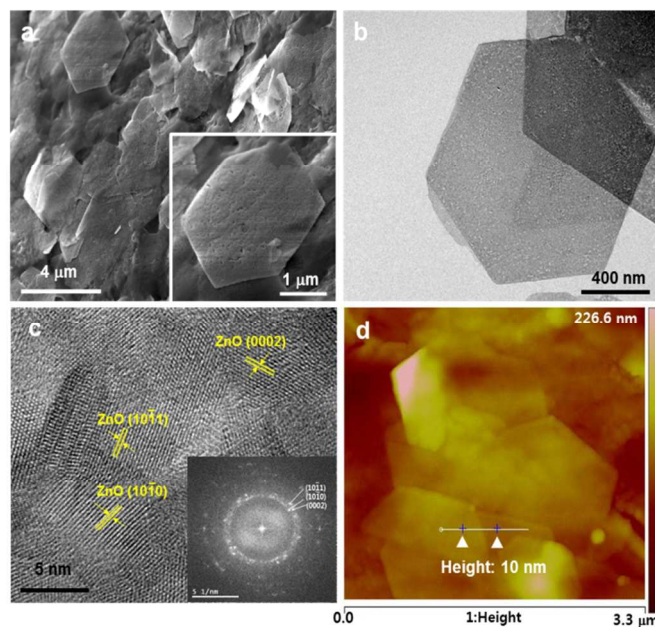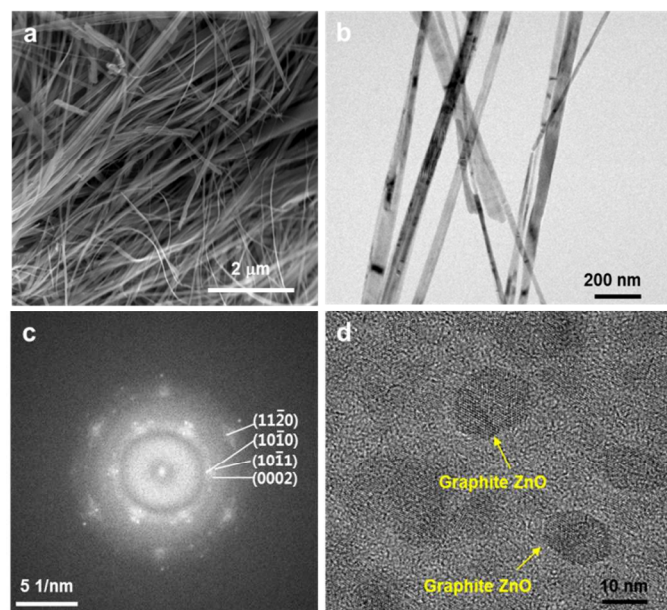

Figure 3. (a) Low-magnification SEM image of a ZnO nanosheet. The inset shows a high-magnification image of the ZnO nanosheet, (b) TEM image of a ZnO nanosheet, (c) HR-TEM images taken of the hexagonal sheet in (b). The inset shows the SAED pattern. (d) AFM image of a hexagonal ZnO nanosheet.

measurements. However, it is clear from the measurements of many sheets that they are unilamellar sheets. This indicates that the precursor with its layered structure was exfoliated by the exfoliation process.

The polar (0001) faces of wurtzite ZnO are electrostatically unstable Tasker type III surfaces that cannot exist without a mechanism to redistribute their surface charge and lower their free energy. It is reasonable to expect that the orientation of ZnO wire is determined by the nucleation and the fastest growth of the c axis. The cation ions of TEFB were neutralized upon the charging of the (000$\bar{1}$) O^{2-}-terminated face. This can accelerate the growth of the c-axis direction on the polar (0001) faces of ZnO and lead to the creation of ZnO nanowire (Figures 4a and 4b). The fairly well-aligned polycrystalline hexagonal nanowires are typically 100-200 nm wide and as long as

approximately 100 μm. The reaction time required for the growth of ZnO nanowire is exceedingly long (usually from several hours to several days). Therefore, a simple and rapid route for the synthesis of ZnO nanowire has remained a great challenge thus far. The result here presents a simple route for the synthesis of ZnO nanowires with long lengths in a short time. The ZnO nanowires were characterized with TEM for a better understanding of their microstructure and mechanism of formation. The labeled lattice directions correspond to the perpendicular $(10\bar{1}0)$ and $(11\bar{2}0)$ planes of ZnO, confirming that the c axis is normal to the membrane surface. This can have implications pertaining to the c-axis orientation of wurtzite thin films and nanowire in general. The weak hexagonal faceting of the ZnO nano-crystalline component is also evident. Selected-area electron diffraction (SAED) was utilized at low magnification to investigate the ZnO nanowire. The SAED pattern in Figure 4c shows strong the (0002) ring, confirming the c axis growth and displaying hexagonally arranged spots. Figure 4d is a lattice-resolved image of the hexagonal ZnO nano-crystalline component on the TEM window. Claeyssens et al.[13] recently found that extremely thin ZnO films may exist in a graphitic arrangement that undergoes a barrier-free transition to the (0001) morphology. Graphite has a layered, planar structure. In each layer, the carbon atoms are arranged in a honeycomb lattice with separation of 0.142 nm, and the distance between the planes is 0.335 nm.[14] In this result, the ZnO nanowire consisted of stacked layers of hexagonal ZnO nanoparticles, like the structure of graphite.

To confirm the anion and cation effect, first, we explored the anion effect by changing the SDS with the lithium dodecyl sulphate (LiDS) and ammonium dodecyl sulphate (NH₄DS)

Figure 4. (a) SEM image of ZnO nanowire, (b) TEM image of ZnO nanowire at low amplification, and (c) the corresponding SAED pattern. (d) HR-TEM image of a ZnO nanowire.
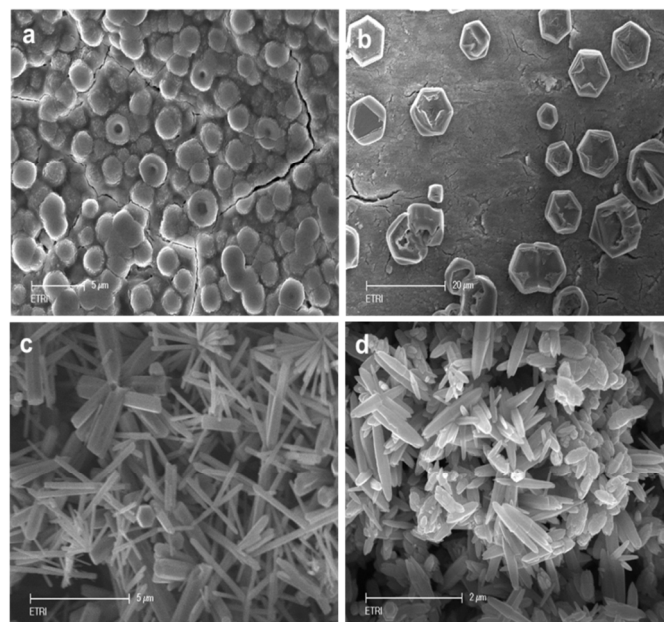

Figure 5. The counter ion effect of few salts on ZnO morphology. (a) lithium dodecyl sulfate, (b) ammonium dodecyl sulphate, and (c) tetraethylammonium chloride. (d) tetraethylammonium hydroxide.

which have the same length of alkyl chain with different counter ions. The size of non-hydrated counter-ions increase in the order $Li^+ < Na^+ < NH_4^+$ but the hydrated ion size shows the reverse order $Li^+ > Na^+ > NH_4^+$ due to the greater hydration of a lithium ion compared to sodium and ammonium ions. The highly charged bare cationic ion becomes a much larger hydrated ion due to the strong binding interaction with water molecules, and it can also be understood that the repulsive forces between similar hydrated ions appear to increase in the order of $Li^+ > Na^+ > NH_4^+$. By exchanging the lithium cation with the sodium cation associated with DS anion, the ZnO obtained is mainly monodisperse hemispheres (Figure 5a) and the edge shape is rough due to the influence of the strong hydrated lithium ion. When the ZnO was synthesized in the NH₄DS condition (Figure 5b), ZnO has a thicker hexagonal structure with a concave center in comparison with those prepared using SDS and LiDS. These results seem to mean that the cationic counter ions (associated with surfactant molecules) influence the ZnO morphology. However, DS anion still maintains their characteristics which anchored onto the Zn^{2+}-terminated (0001) plane and suppressed the c-axis growth. We executed the same experiment for the counter ion effect of cation. We have used the tetraethylammonium chloride (TEC) and tetraethylammonium hydroxide (TEH) instead of TEFB to see the counter ion effect. ZnO obtained from bathes containing TEC was mainly rod-like (Figure 5c) while crystallites obtained from baths containing TEH were pencil shaped nanorods at the front and back side (Figure 5d). These results indicate that, even though ZnO morphology was changed by the counter ions effect, tetraethylammonim cations have the innate property to grow the c-axis orientation of ZnO. We will further study ionic

effect on ZnO morphology to prove the ZnO growth mechanism exactly.

The crystallinity and crystal size of the ZnO were analyzed using XRD. Figure 6 shows the $(10\bar{1}0)$, (0002), and $(10\bar{1}1)$ XRD peaks of ZnO (JCPDS card No. 36-1451). Well-aligned crystallographic faces, i.e., polar-terminated (0001) and non-polar low-symmetry $(10\bar{1}1)$ faces (and C6v symmetric ones) can clearly be identified. These correspond to the typical crystal habit and growth form of the ZnO hexagonal wurtzite structure (P63mc, a = b = 3.2489 Å, c=5.2049 Å). As shown in Figure 5, the XRD analysis revealed that all of the ZnO samples showed
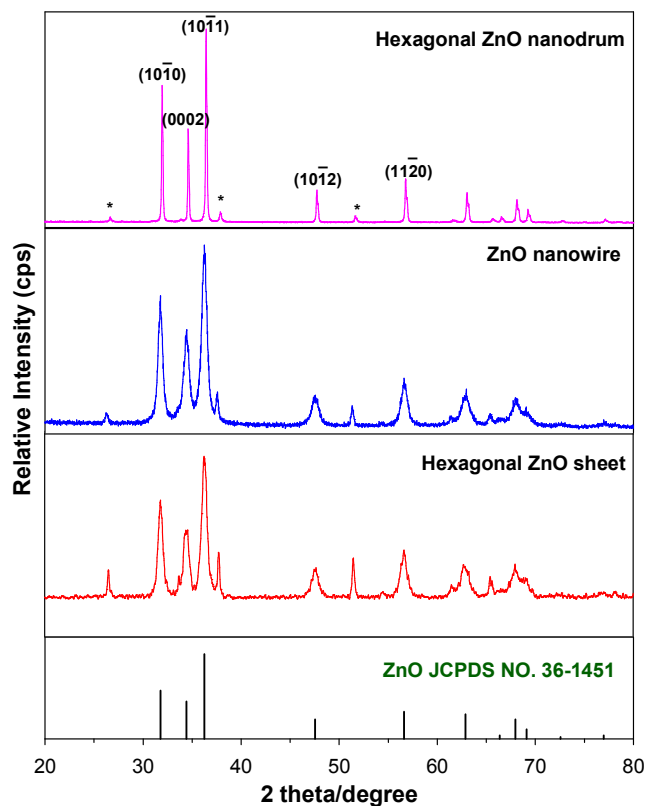
Figure 6. X-ray diffraction of the hexagonal ZnO nanodrum, nanosheet and nanowire as obtained by a heat treatment at 350 °C. Reflections indexed to crystalline ZnO (zincite, JCPDS card no. 36-1451). * Signal arising from the fluorine-tin-oxide (FTO) substrate.

enhanced (0002) and $(10\bar{1}0)$ peaks from the ZnO crystal hexagonal structure and preferred orientation with c-axis growth.[15]

The optical properties of ZnO were obtained by means of PL measurements (Figure 7). All ZnO nanostructures exhibited weak band-edge emission at ~380 nm resulting from free-exciton annihilation,[16] and the green light emission intensity at ~520 nm attributed to the creation of oxygen vacancies.[17] Whilst the UV emission corresponds to the near band-edge emission, the green emission peak is commonly referred to as a type of deep-level or trap-state emission. The green transition is attributed to the singly ionized oxygen vacancy in ZnO
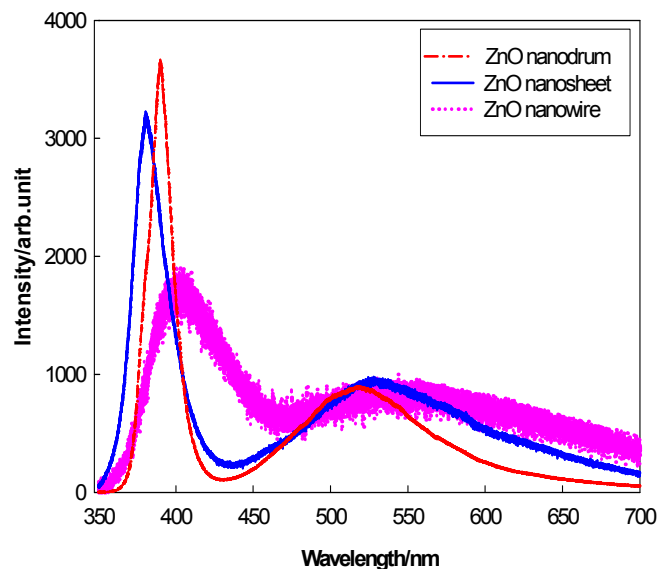
Figure 7. (a) Photoluminescence spectra of the hexagonal ZnO nanodrum, nanosheet and nanowire

resulting from the radiative recombination of a photogenerated hole with an electron occupying the oxygen vacancy.[18] A slight red shift of the near band-edge emission as well as an increase in the peak intensity was observed in the ZnO nanodrum and ZnO nanowire in comparison to the ZnO nanosheet. These findings were ascribed to the presence of stimulated emission[19] and to the heating effect of the excitation light.[20]

To get clearer information about the ZnO nanostructures, we further investigated the structures of the ZnO for the potential application of dye-sensitized solar cells (DSSCs). We demonstrated the use of the ZnO nanostructures as photoanodes for DSSCs by transferring the ZnO to the FTO substrates. Figure 8 displays the IPCE spectra for the ZnO electrodes. IPCE can be expressed in terms of the light-harvesting efficiency (LHE), the quantum yield of charge injection form the excited dye to the semiconductor (Φ_{inj}), and the collection efficiency of injected electrons at the back contact (ηc) by means of the equation of IPCE (λ) = LHE$(\lambda) \cdot \Phi_{inj} \cdot \eta$c. The light harvesting efficiency can be calculated from the equation LHE(λ) = $1-10^{-\Gamma\sigma(\lambda)}$, where Γ is the surface concentration of dye molecules and σ is the absorption cross section. The maximum IPCE (at 530 nm) of 20% was obtained for ZnO nanowire among the ZnO nanostructures. Therefore, ZnO nanowires assembled from connected nanoparticles allows more efficient transport and collection of photogenerated electrons through a designed path.[21] The low IPCE values for dye-sensitized ZnO nanosheet cell must therefore be attributed to poor electron injection efficiency.

Figure 9 shows the current (Jsc)-voltage (V) result for the ZnO nanostructure fabricated DSSCs. Table 1 summarizes the short circuit current density (Jsc), the open circuit voltage (Voc), the fill factor (FF), and the overall conversion efficiency (η) for all
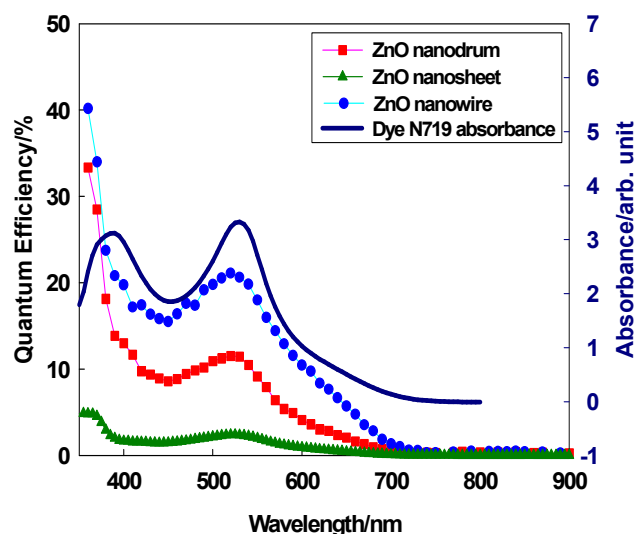
Figure 8. IPCE spectra for hexagonal ZnO nanodrum, nanosheet and nanowire photoelectrode
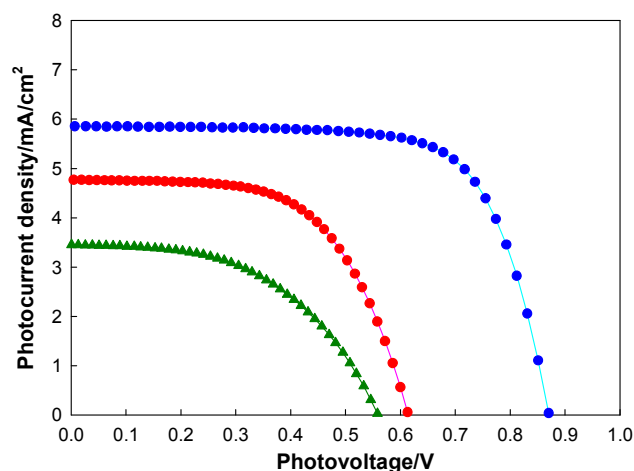

Figure 9. The I-V curves for DSSCs fabricated from hexagonal ZnO nanodrum, nanosheet and nanowire

centers for the electron transport and therefore affect the performance of the film. This was investigated by intensity-modulated photocurrent spectroscopy (IMPS) and intensity-modulated photovoltage spectroscopy (IMVS). Figure 10 shows diffusion coefficient and electron life time of ZnO nanostructures for a photon intensity level from 20 W/m^2 to 80 W/m^2 with the IMPS and IMVS experiments. An order of magnitude estimate of the mean transit time for photogenerated electrons can be obtained from the frequency minimum in the complex-plane IMPS plot: $\tau_d = (2\pi f_{min}(IMPS))^{-1}$,[22] which gives an estimation of the average time that photogenerated electrons need to reach the back contact. In this result, τ_d for the ZnO nanowire was shorter than that of ZnO nanodrum and nanosheet devices, implying that that fast photoelectron collection occurred in the ZnO nanowire devices as compared to the ZnO nanodrum and nanosheet ones. At a short circuit and for homogeneously absorbed light, the electron diffusion coefficient can be estimated from the relationship $D_n = d^2/4\tau_d$, where d is the layer thickness of the nanocrystalline ZnO. As shown in Figure 10, the electron diffusion coefficient (D_n) of
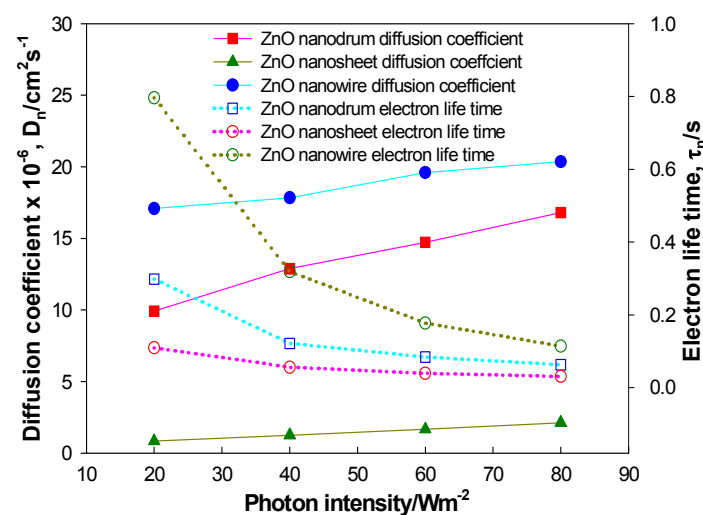

Figure 10. Light intensity dependence of the electron lifetime and diffusion coefficient of ZnO nanodrum, nanosheet and nanowire based solar cells with N719 from the IMVS and IMPS experiment, respectively. The photon intensity was ranged from 20 W m^{-2} to 80 W m^{-2}.

ZnO nanostructures. ZnO nanowire cell present the highest conversion efficiency of all the samples 3.62%, approximately 105% higher than the efficiency of 1.76% achieved for the ZnO nanodrum cell and 273% higher than the efficiency of 0.97% for the ZnO nanosheet one. Similarly, the largest short-circuit current density of 5.86 mA cm^{-1}, achieved for the ZnO nanowire cell, is 23% higher than that of 4.76 mA cm^{-1} for the ZnO nanodrum cell, and 70% higher than that of 3.45 mA cm^{-1} for the ZnO nanosheet one. These results can be explained as a consequence of reduced recombination due to the direct path way of the ZnO nanowire for the electron transport.

  The reactive surface facet of the ZnO nanowire can be expected to decrease the surface trap sites and recombination

the ZnO nanowire cell is also higher compared to that of the ZnO nanodrum and nanosheet ones. This may be credited to the effective charge screening in the ZnO nanowire, which stemmed from the decrease in the number of recombination sites and the resulting rapid movement of the electron. The electron lifetime can be obtained from an IMVS plot by setting $\tau_n = (2\pi f_{min}(IMVS))^{-1}$.[22] It is clear from Figure 10 that the electron lifetime (τ_n) of the ZnO nanowire cell is much longer than that of the ZnO nanodrum and nanosheet cells. This suggests that the ZnO nanowire surface decreases the presence of dye molecules at surface sites or trap sites, where photogenerated electrons can be trapped, while also

recombining with the I_3^- in the electrolyte, which suppresses recombination and leads to a longer electron lifetime.

3. Conclusions

In summary, the hexagonal ZnO crystal has six polar and two non-polar faces. The growth of a certain surface can be impeded by additives which preferentially adsorb onto specific crystal surface. Using this characteristic, we could synthesize ZnO nanodrums, nanosheets and nanowires in the hexagonal ZnO growth condition by replacing the favorably absorbed ions with ZnO reactive facets. When the ZnO nanostructures were applied to the photovoltanic devices, the cell performances were dependent on the ZnO nanostructures. Among the ZnO nanosturctures, ZnO nanowire solar cell shows the most effective transport of electron, which increased the cell efficiency.

4. Experimental Section

Synthesis of ZnO: For the preparation of the ZnO nanodrums, a 25 mM equimolar concentration of zinc nitrate hexahydrate $(Zn(NO_3)_2 \cdot 6H_2O)$ and hexamethylenetramine (HMTA) was prepared in 100 mL of deionized Milli-Q water. 2 wt% of a nonionic surfactant, polyethylene glycol *tert*-octylphenyl ether (Triton X-100), was added to the solution and the resulting suspension was stirred vigorously for 2 h. The resulting milky white mixture was transferred to an autoclave made of titanium. The temperature of the autoclave was held at 90 ^{o}C for 24 h. After the reaction, the precipitates obtained were centrifuged, washed several times with ethanol, and baked in air at 350 ^{o}C for 1 h to remove any residual organics. The ZnO hexagonal nanosheets and nanowire were prepared in 100 mL of 25 mM equimolar zinc nitrate hexahydrate and HMTA containing of 2 wt% SDS and TEFB, respectively, using the same procedure to create the ZnO nanodrums. We executed additional experiments for the cation and anion effect by the changing their counter ions using the LiDS, NH₄DS, TEC and THE in the same experimental condition.

Characterizations: SEM images of the ZnO were obtained with a field-emission scanning electron microscope (FEI, Model: Sirion, Netherlands). Field-emission transmission electron microscopy (FE-TEM) images were obtained with a JEM-2100F instrument (JEOL Ltd., Japan). Atomic force microscopy (AFM) measurements were carried out on a Digital Instruments Multimode AFM with the Nanoscope IV design operating in tapping mode with silicon cantilevers (resonance frequency in the range of 204-259 kHz, an integrated Si tip with a typical radius of curvature of 10 nm). XRD patterns were measured using a D8 Discover thin-film diffractometer with Cu Kα radiation (40 kV, 30 mA, λ = 1.54056 Å) and a Ni filter plus a graphite monochromator. The XRD spectrum was recorded in a Bragg-Brentano configuration using θ/2θ scanning and no tilt angle. Photoluminescence (PL) measurements (model; LabRAM HR UV-Visible-NIR, France, Horiba Jobin Yvon) of the ZnO arrays were performed using a 325 nm line and with a 1800 grating of a He-Cd laser as the excitation source at room temperature.

Device Fabrication: When we fabricated the ZnO photoanodes, we have used the pure and same amount of ZnO nanostructures. After ZnO was dispersed in the ethanaol (ZnO: ethanol=1:1 wt%), a few drops of the resultant ZnO solution were then placed onto the fluorine-tin-oxide (FTO, 3 mm, 10 Ω/square, Pilkington TEC8) substrates and the films were formed by a doctor-blading process. The films were dried and then immediately heat treated at a temperature of 350 °C for 1 h, forming a layer of white film during the quick evaporation of the solvent. In this study, all ZnO nanostructures have nearly the same thickness, 5 μm. To absorb the dye, ZnO substrates were then immersed in a 0.3 mM $(Bu_4N)_2$- ("N719", Solaronix) in ethanol for 30 min. To prepare Pt counter-electrodes, 10 mM hydrogen hexachloroplatinate(IV) hydrate $(H_2PtCl_6$, Aldrich, 99.9%) in a 2-propanol solution was coated on FTO glass, followed by heating at 450 ^{o}C for 30 min. The dye adsorbed ZnO electrode and Pt counter-electrode were assembled into a sealed sandwich-type cell by heating with a hot melt of a 50 μm thick Surlyn polymer film (Surlyn, Dupont 1702). A electrolyte solution of 0.6 M tetra-butylammonium iodide, 0.1 M lithium iodide, 0.1 M iodide and 0.5 M 4-tert-butyl pyridine in acetonitrile was introduced into holes drilled in the counter-electrode of the assembled cell, followed by sealing the holes using a microcover glass and Surlyn.

Photovoltaic measurements: The photocurrent (Jsc) and photovoltage (Voc) of the DSSCs were measured with an active area of 0.15-0.25 cm^2 using simulated solar light at AM 1.5, produced by a 1000 W xenon lamp (Oriel, 91193). Its irradiant power was adjusted with respect to Si reference solar cell (Fraunhofer Institute for Solar Energy System: Mono-Si + KG filter) to about one-sun light intensity (100 mW/cm^2). IPCE was measured using a system designed by PV measurement. A 12 W halogen lamp was applied as the light source for the monochromatic beam. For its calibration, a silicon photodiode (NIST-calibrated photodidode G425) was used. Incident photon to current efficiency (IPCE) data was obtained at a low chopping speed of 5 Hz and the quantum efficiency was detected by a lock in amplifier. The IMVS and IMPS measurements were performed on a ZAHNER CIMPS system. A stationary DC voltage and a concurrent sinusoidal modulated AC voltage were imposed on a green LED, which gave out a green irradiance with a maximum wavelength at 525 nm. The LED was controlled by a potentiostatic feedback loop. The selected AC amplitude ranged from 5% to 15% of the stationary DC value. The transfer functions of IMPS and IMVS were determined by correlating the system response with the actual stimulation signal. The potential applied to the testing cell was controlled by a potentiostat unit. IMPS measurement was carried out under short-circuit condition while IMVS measurement was carried out under open-circuit condition. The measured short circuit photocurrent efficiency (Φext(ω)) of IMPS and the real and imaginary parts of modulated photovoltage ΔVoc of IMVS were fitted by using the Levenberg-Marquardt algorithm.

22 J. Krüger, R. Plass, M. Grätzel, P. J. Cameron and L. M. Peter, *J. Phys. Chem. B*, 2003, **107**, 7536; M.-H. Jung, M.-J. Chu and M. G. Kang, *Chem. Commun.*, 2012, **48**, 5016.

Acknowledgements

Notes and references

ª Solar Cell Technology Research Section, IT Components and Materials Industry Technology Research Department, IT Materials and Components Laboratory, Electronics and Telecommunications Research Instituteline, 218 Gajeongno, Yuseong-gu, Daejeon, 305-700, Republic of Korea, E-mail: mhjung@etri.re.kr.

1 M.-H. Jung and H. Lee, *Nanoscale Res. Lett.*, 2011, **6**, 1.

2 K. Govender, D. S. Boyle, P. B. Kenway and P. O'Brien, *J. Mater. Chem.*, 2004, **14**, 2575.

3 Z. R. Tian, J. A. Voigt, J. Liu, B. McKenzie, M. J. McDermott, M. A. Rodriguez, H. Konishi and H. Xu, *Nat. Mater.*, 2003, **2**, 821.

4 P. W. Tasker, *J. Phys. C: Solid State Phys.*, 1979, **12**, 4977.

5 K. S. Krishna, G. Vivekanandan, D. Ravinder and M. Eswaramoorthy, *Chem. Commun.*, 2010, **46**, 2989.

6 F. Li, Y. Ding, P. Gao, X. Xin and Z. L. Wang, *Angew. Chem. Int. Ed.*, 2004, **43**, 5238.

7 A. Dev, S. K. Panda, S. Kar, S. Chakrabarti and S. Chaudhuri, *J. Phys. Chem. B*, 2006, **110**, 14266.

8 S. Crook, H. Dhariwal and G. Thornton, *Surf. Sci.*, 1997, **382**, 19.

9 J. Zhang, H. Liu, Z. Wang, N. Ming, Z. Li and A. S. Biris, *Adv. Funct. Mater.*, 2007, **17**, 3897.

10 H. Kato, M. Sano, K. Miyamoto and T. Yao, *J. Cryst. Growth*, 2004, **265**, 375.

11 T. Sasaki, Y. Ebina, M. Watanabe and G. Decher, *Chem. Commun.*, 2000, 2163; M. Muramatsu, K. Akatsuka, Y. Ebina, K. Wang, T. Sasaki, T. Ishida, K. Miyake and M.-a. Haga, *Langmuir*, 2005, **21**, 6590.

12 S. Ida, D. Shiga, M. Koinuma and Y. Matsumoto, *J. Am. Chem. Soc.*, 2008, **130**, 14038.

13 F. Claeyssens, C. L. Freeman, N. L. Allan, Y. Sun, M. N. R. Ashfold and J. H. Harding, *J. Mater. Chem.*, 2005, **15**, 139.

14 P. Delhaes *Graphite and precursors*; Gordon & Breach: Amsterdam 2001.

15 W.-J. Li, E.-W. Shi, W.-Z. Zhong and Z.-W. Yin, *J. Cryst. Growth*, 1999, **203**, 186.

16 X. Gao, X. Li and W. Yu, *J. Phys. Chem. B*, 2005, **109**, 1155.

17 D. Wang and C. Song, *J. Phys. Chem. B*, 2005, **109**, 12697; X. L. Wu, G. G. Siu, C. L. Fu and H. C. Ong, *Appl. Phys. Lett.*, 2001, **78**, 2285.

18 K. Vanheusden, W. L. Warren, C. H. Seager, D. R. Tallant, J. A. Voigt and B. E. Gnade, *J. Appl. Phys.*, 1996, **79**, 7983.

19 P. Zu, Z. K. Tang, G. K. L. Wong, M. Kawasaki, A. Ohtomo, H. Koinuma and Y. Segawa, *Solid State Commun.*, 1997, **103**, 459; D. M. Bagnall, Y. F. Chen, M. Y. Shen, Z. Zhu, T. Goto and T. Yao, *J. Cryst. Growth*, 1998, **184**, 605.

20 Y. J. Xing, Z. H. Xi, Z. Q. Xue, X. D. Zhang, J. H. Song, R. M. Wang, J. Xu, Y. Song, S. L. Zhang and D. P. Yu, *Appl. Phys. Lett.*, 2003, **83**, 1689.

21 M. Law, L. E. Greene, J. C. Johnson, R. Saykally and P. Yang, *Nat. Mater.*, 2005, **4**, 455.